

Research Paper

# Copper Manganese Sulfide Nanoplates: A New Two-Dimensional Theranostic Nanoplatform for MRI/MSOT Dual-Modal Imaging-Guided Photothermal Therapy in the Second Near-Infrared Window

Kaimei Ke<sup>1</sup>, Wen Yang<sup>1</sup>, Xiaoli Xie<sup>2</sup>, Rui Liu<sup>2</sup>, Li-Li Wang<sup>3</sup>, Wei-Wen Lin<sup>3</sup>, Guoming Huang<sup>2</sup>, Chun-Hua Lu<sup>1</sup>✉ and Huang-Hao Yang<sup>1</sup>✉

1. MOE Key Laboratory for Analytical Science of Food Safety and Biology, State Key Laboratory of Photocatalysis on Energy and Environment, College of Chemistry, Fuzhou University, Fuzhou 350116, P. R. China;
2. College of Biological Science and Engineering, Fuzhou University, Fuzhou 350116, P. R. China;
3. Department of Diagnostic Radiology, Union Hospital, Fujian Medical University, Fuzhou 350001, P. R. China.

✉ Corresponding authors: chunhualu@fzu.edu.cn; hhyang@fzu.edu.cn

© Ivyspring International Publisher. This is an open access article distributed under the terms of the Creative Commons Attribution (CC BY-NC) license (<https://creativecommons.org/licenses/by-nc/4.0/>). See <http://ivyspring.com/terms> for full terms and conditions.

Received: 2017.06.29; Accepted: 2017.08.27; Published: 2017.10.17

## Abstract

Multifunctional nanoplatforms with integrated diagnostic and therapeutic functions have attracted tremendous attention. Especially, the second near-infrared (NIR-II) light response-based nanoplatforms hold great potential in cancer theranostic applications, which is because the NIR-II window provides larger tissue penetration depth and higher maximum permissible exposure (MPE) than that of the well-studied first near-infrared (NIR-I) window. Herein, we for the first time present a two-dimensional (2D)-nanoplatform based on  $\text{Cu}_2\text{MnS}_2$  nanoplates (NPs) for magnetic resonance imaging (MRI)/multispectral optoacoustic tomography (MSOT) dual-modal imaging-guided photothermal therapy (PTT) of cancer in the NIR-II window. **Methods:**  $\text{Cu}_2\text{MnS}_2$  NPs were synthesized through a facile and environmentally friendly process. A series of experiments, including the characterization of  $\text{Cu}_2\text{MnS}_2$  NPs, the long-term toxicity of  $\text{Cu}_2\text{MnS}_2$  NPs in BALB/c nude mice, the applications of  $\text{Cu}_2\text{MnS}_2$  NPs for *in vitro* and *in vivo* MRI/MSOT dual-modal imaging and NIR-II PTT of cancer were carried out. **Results:** The as-synthesized  $\text{Cu}_2\text{MnS}_2$  NPs exhibit low cytotoxicity, excellent biocompatibility as well as high photothermal conversion efficiency (~49.38%) and outstanding photostability. Together with their good  $T_1$ -shortening effect and strong absorbance in the NIR-I and NIR-II region, the  $\text{Cu}_2\text{MnS}_2$  NPs display high-contrast imaging performance both in MRI and MSOT (900 nm laser source). Moreover, the subsequent *in vitro* and *in vivo* results demonstrate that the  $\text{Cu}_2\text{MnS}_2$  NPs possess excellent PTT efficacy under 1064 nm laser irradiation with a low power density ( $0.6 \text{ W cm}^{-2}$ ). In addition, the detailed long-term toxicity studies further confirming the safety of  $\text{Cu}_2\text{MnS}_2$  NPs *in vivo*. **Conclusion:** We have developed a new 2D  $\text{Cu}_2\text{MnS}_2$  NPs as multifunctional theranostic agents for MRI/MSOT dual-modal imaging-guided PTT of cancer in the NIR-II window. Such biocompatible  $\text{Cu}_2\text{MnS}_2$  NPs might provide a new perspective for exploring new 2D-based nanoplatforms with improved properties for clinical applications in the future.

Key words: two-dimensional nanomaterial, copper manganese sulfide nanoplates, MRI/MSOT dual-modal imaging, second near-infrared window, photothermal therapy.

## Introduction

Photothermal therapy (PTT) is regarded as a promising cancer treatment strategy which utilizes photoabsorbing agents to convert laser light energy

into heat to burn cancer cells [1-3]. Compared with traditional cancer therapies, such as radiotherapy and chemotherapy, PTT is a non-invasive technique for

tumor ablation without damaging surrounding normal cells or organs in preclinical trials [4-6]. An enormous amount of studies have focused on pursuing new agents with higher photothermal conversion efficiency [7-9]. However, only a few of studies specialized on the excitation wavelength of the NIR-absorbing agents [10]. The laser wavelengths used in PTT are highly depended on the absorbent range of the NIR-absorbing agents. Because of the low scattering and energy absorption of tissue transmission, NIR light displays much deeper tissue penetration depths than that of ultraviolet-visible (UV-vis) light [11, 12]. In the NIR region, there are two so-called biological transparency windows: the first biological window (NIR-I, from 650 nm to 950 nm) and the second biological window (NIR-II, from 1000 nm to 1350 nm) [13]. NIR-II window exhibits two advantages compared with the well-researched NIR-I window: deeper penetration depths in tissue and higher maximum permissible exposure (MPE) of laser [14]. In particular, the penetration depth is expected to be maximal in the spectral ranges 1000-1100 nm [15]. Moreover, according to the "American National Standard for Safe Use of Lasers" (ANSI Z136.1-2007), the MPE for skin exposure is  $1 \text{ W cm}^{-2}$  at 1064 nm, while the value is  $0.33 \text{ W cm}^{-2}$  at 808 nm. To date, various nanomaterials or nanostructures have been used as PTT agents in NIR-I range [16-21]. Although the nanomaterials capable of emitting NIR-II light have been received some attention in biological imaging [22-24], rare reports have demonstrated that these nanomaterials could act as PTT agents in the NIR-II region [25].

Recently, several groups have successfully developed nanoplatfoms for NIR-II responsive PTT [14, 26-31]. However, there are still some issues need to be addressed. For instance, these nanomaterials are usually synthesized in oxygen-free atmosphere, typically coated with hydrophobic ligands during the synthesis process and hence are water insoluble [14, 26-28, 30]. Therefore, a further surface modification or phase transfer step is required to render products water-soluble for biomedical applications [31]. Facile synthesis of NIR-II responsive PTT agents with good biocompatibility remains challenging. Furthermore, the usage power of laser of current NIR-II agents is much higher than MPE [25, 27], which might hinder their applications in the PTT of cancer. In this regard, the development of PTT agents with strong absorption in the NIR-II window, which could generate enough heat irradiated by laser with low power density, thus becomes extremely important.

Although the PTT of cancer possess substantial advances, this technique cannot provide more information of tumor conditions. In order to evaluate

the therapeutic effects of PTT, an alternative strategy is using imaging-guided combination therapy to monitor real-time visualization of PTT [32]. Magnetic resonance imaging (MRI), a facile, non-invasive and powerful nuclear magnetic resonance (NMR)-based imaging modality, has been widely applied in clinic for disease diagnosis since MRI is able to obtain three-dimensional (3D) tomographical information with high temporal-spatial resolution in whole tissue samples [33]. However, the poor sensitivity of MRI may hinder its application for accurate cancer diagnosis [34]. Multimodal imaging which combines two or more imaging techniques could integrates the superiorities of each imaging techniques while avoiding their defects, thus becoming a desirable demand [35]. For instance, multispectral optoacoustic tomography (MSOT), which combines the best features of optical- and ultrasonic-imaging, is an emerging and promising imaging technique. MSOT has distinct advantages, including high sensitivity, non-ionization and background-free detection [36, 37]. Therefore, combining MRI and MSOT for dual-modal imaging with the advantages of high resolution (10–100  $\mu\text{m}$ ) and deep penetration (up to 50 mm) as well as high sensitivity ( $\sim 10^{-9} \text{ mol L}^{-1}$ ) is considered to be a promising approach for accurate cancer diagnosis [38-43]. Up to now, many efforts have been devoted to develop nanoplatfoms with both imaging and therapy properties [44-46]. Among these, two-dimensional (2D) nanomaterials-based theranostic platforms have attracted great attention to reaserchers because of their special compositional, structural and physical/chemical properties [47-50]. To further enhance the performance of their application in imaging-guided PTT, these 2D nanomaterials are usually hybridized with other functional elements or structures [51, 52]. However, current studies are mainly focused on the PTT in NIR-I window, and no relevant reports regarding the theranostic effect of 2D nanomaterials in the NIR-II window.

Inspired by the great potential of the 2D nanomaterial for biomedical applications, we for the first time present a 2D-nanoplatfom based on  $\text{Cu}_2\text{MnS}_2$  nanoplates (NPs) for MRI/MSOT dual-modal imaging-guided PTT of cancer in the NIR-II window (**Figure 1**).  $\text{Cu}_2\text{MnS}_2$  NPs were synthesized using a facile and effective one-pot solvothermal method by adjusting the proportion of Cu/Mn/S. The as-synthesized  $\text{Cu}_2\text{MnS}_2$  NPs exhibit low cytotoxicity, high photothermal conversion efficiency and  $T_1$ -shortening effect, excellent photostability and strong absorbance in NIR-I and NIR-II region. Taking advantage of the above properties, the  $\text{Cu}_2\text{MnS}_2$  NPs could be a promising

contrast agent for MRI/MSOT dual-modal imaging-guided PTT of cancer. Furthermore,  $\text{Cu}_2\text{MnS}_2$  NPs can effectively kill cancer cells both *in vitro* and *in vivo* under the 1064 nm laser irradiation with a low power density ( $0.6 \text{ W cm}^{-2}$ ). Therefore, the 2D-nanomaterial  $\text{Cu}_2\text{MnS}_2$  NPs could be used as an attractive multifunctional platform for simultaneous MRI/MSOT imaging and NIR-II PTT, holding great promise in biomedical applications.

## Results and Discussion

### Synthesis and Characterization of $\text{Cu}_2\text{MnS}_2$ NPs

The synthetic strategy is based on a facile one-pot solvothermal route involving ethylene glycol (EG), monomethoxycarboxyl polyethylene glycol (mPEG-COOH),  $\text{CuCl}_2 \cdot 2\text{H}_2\text{O}$ ,  $\text{MnCl}_2 \cdot 4\text{H}_2\text{O}$  and  $\text{Na}_2\text{S}$ , where EG was the reactive solvent and mPEG-COOH was the capping agent as well as the stabilizing agent.

As shown in **Figure 2a** and **Figure S1**, nanoplates (NPs) can be obtained by optimizing experimental conditions (See “Materials and Methods” section). The as-synthesized product showed well-defined uniform NPs with a diameter around 100 nm (**Figure 2a**). The observed lattice spacing in the high-resolution TEM (HRTEM) image is about 0.259 nm for the (111) plane of NPs (**Figure 2a**, Insert). The hydrodynamic size of the NPs was about 120 nm determined by dynamic light scattering (DLS) (**Figure 2b**). The atomic force microscopy (AFM) images also demonstrated that most NPs had a diameter of about 100 nm and a thickness of approximately 6 nm, confirming the layered structure of NPs (**Figure 2c, d**). The chemical composition of NPs was then investigated by energy dispersive X-ray spectroscopy (EDS). EDS analysis and elemental distribution mappings clearly indicated the existence of Cu, Mn and S elements in the NPs with the atomic ratio of Cu : Mn : S to be 2.03 : 1 : 1.99 (**Figure 2e,f**). The structure of

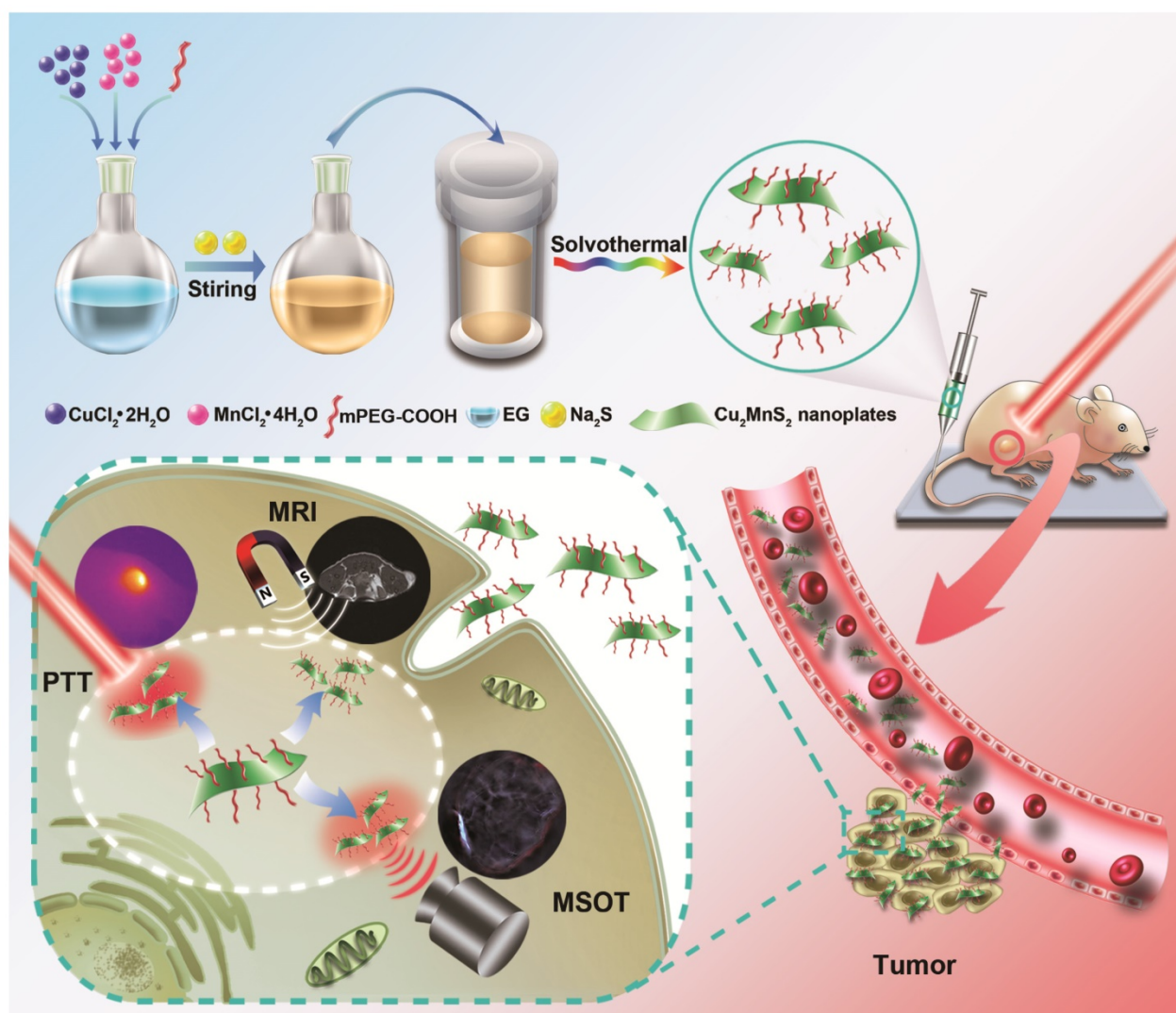


**Figure 1.** Schematic illustration for the syntheses and applications of  $\text{Cu}_2\text{MnS}_2$  NPs as a theranostic platform.

the NPs was also confirmed by X-ray powder diffraction (XRD), which matches well with the standard powder diffraction pattern of  $\text{Cu}_2\text{MnS}_2$  (JCPDS No. 50-0540) (Figure 2g). Furthermore, Cu, Mn and S were detected in the X-ray photoelectron spectroscopy (XPS) spectra (Figure 2h and Figure S2). Moreover, the mPEG-COOH could bind to the  $\text{Cu}_2\text{MnS}_2$  NPs through Cu-carboxylate coordinative couplings [53]. The characteristic bond vibrations illustrated in Fourier-transform infrared spectroscopy (FTIR) (Figure S3a) of the  $\text{Cu}_2\text{MnS}_2$  NPs showed the typical peaks at  $\sim 1110\text{ cm}^{-1}$  (C-O-C),  $\sim 1660\text{ cm}^{-1}$  (C=O),  $\sim 2875\text{ cm}^{-1}$  (C-H) and  $\sim 3400\text{ cm}^{-1}$  (O-H), confirming the successful surface grafting of mPEG-COOH [54]. A weight loss of 13.7%, which could be attributed to the grafted mPEG-COOH chains, was calculated from the thermogravimetric analysis (TGA) curve of  $\text{Cu}_2\text{MnS}_2$  NPs (Figure S3b).

The zeta-potential ( $\zeta$ ) result with a negatively charged of  $-15.5 \pm 3.6\text{ mV}$  further confirming the surface grafting of mPEG-COOH on the  $\text{Cu}_2\text{MnS}_2$  NPs (Figure S4). Furthermore, the as-synthesized  $\text{Cu}_2\text{MnS}_2$  NPs exhibited excellent dispersibility and stability in water and physiological solutions (Figure S5) owing to the surface-grafted mPEG-COOH chains. The DLS analyses showed that the hydrodynamic diameters of  $\text{Cu}_2\text{MnS}_2$  NPs in different solutions did not change over 30 days (Figure S5), indicating the excellent colloidal stability of  $\text{Cu}_2\text{MnS}_2$  NPs. Notably, the UV-vis-NIR spectrum showed that the  $\text{Cu}_2\text{MnS}_2$  NPs displayed strong absorption from 800 to 1300 nm with peaks at  $\sim 900\text{ nm}$ ,  $\sim 1075\text{ nm}$  and  $\sim 1260\text{ nm}$  (Figure 2i). This result indicated that the as-synthesized  $\text{Cu}_2\text{MnS}_2$  NPs could be as a candidate agent for PTT in the NIR-II biological window.

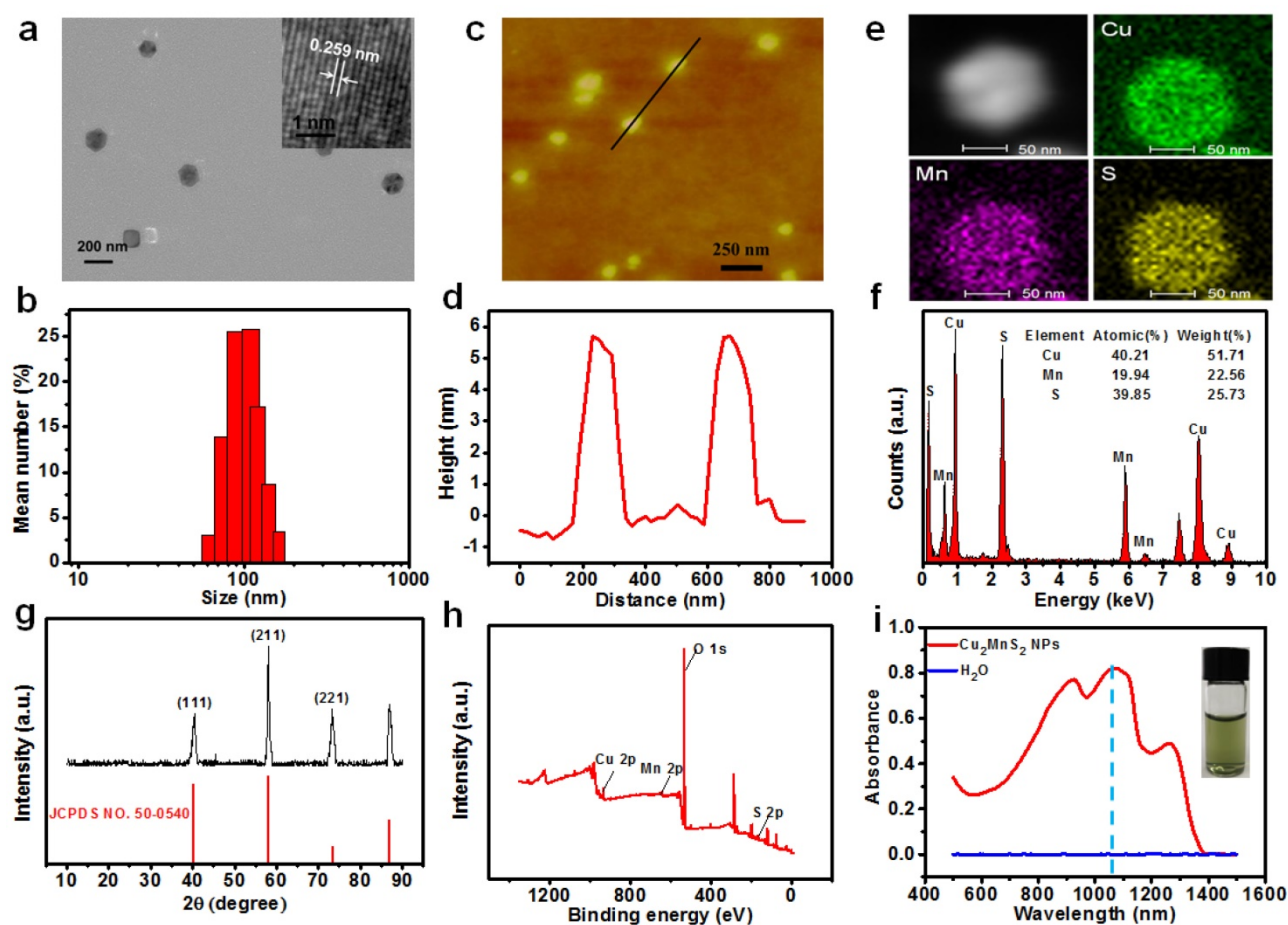


**Figure 2.** (a) TEM image of  $\text{Cu}_2\text{MnS}_2$  NPs (Inset: HRTEM image of  $\text{Cu}_2\text{MnS}_2$  NPs). (b) The diameter distribution of  $\text{Cu}_2\text{MnS}_2$  NPs by DLS test. (c) Atomic force microscopy (AFM) image and (d) the corresponding height analysis of  $\text{Cu}_2\text{MnS}_2$  NPs. (e) STEM-EDS elemental mapping, (f) EDS analysis spectrum, (g) XRD patterns, and (h) XPS spectrum of  $\text{Cu}_2\text{MnS}_2$  NPs. (i) UV-vis-NIR absorption spectrum of  $\text{Cu}_2\text{MnS}_2$  NPs in water. Inset: photograph of  $\text{Cu}_2\text{MnS}_2$  NPs aqueous solution.

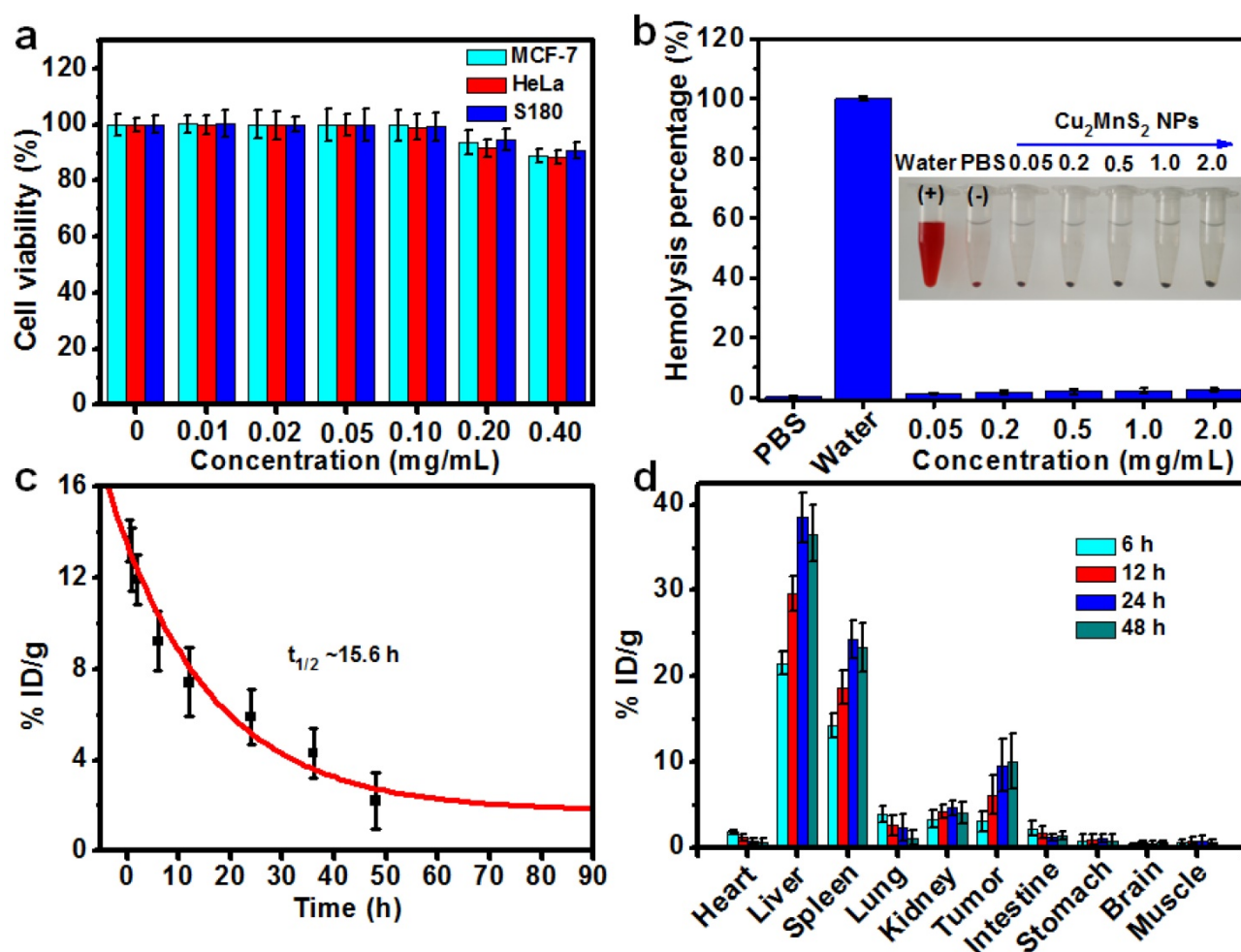


**Figure 3.** (a) Cell viabilities of MCF-7, HeLa and S180 cells after incubated with different concentrations of  $\text{Cu}_2\text{MnS}_2$  NPs for 24 h. (b) The percentages of hemolysis by different concentrations of  $\text{Cu}_2\text{MnS}_2$  NPs. PBS and water were used as negative and positive controls. Insert: photograph of Eppendorf-tubes containing the supernatant from RBCs exposed to different concentrations of  $\text{Cu}_2\text{MnS}_2$  NPs. (c) Blood clearance of  $\text{Cu}_2\text{MnS}_2$  NPs in mice ( $n = 5$ ). (d) Biodistribution of  $\text{Cu}_2\text{MnS}_2$  NPs in tumors-bearing mice at 6 h, 12 h, 24 h and 48 h post-injection, measured by ICP-OES analysis of Mn in different organs and tissues ( $n = 5$ ).

### **In vitro cytotoxicity and in vivo biodistribution study of $\text{Cu}_2\text{MnS}_2$ NPs**

In order to explore the applications of  $\text{Cu}_2\text{MnS}_2$  NPs in biomedicine, we then tested their cytotoxicity on several types of cells by standard cell counting kit-8 (CCK-8) assays. The results revealed that  $\text{Cu}_2\text{MnS}_2$  NPs show low cytotoxicity to these cells even at concentration up to  $400 \mu\text{g mL}^{-1}$  (Figure 3a), indicating good biocompatibility of the  $\text{Cu}_2\text{MnS}_2$  NPs. Efficient cellular uptake and internalization of the  $\text{Cu}_2\text{MnS}_2$  NPs are paramount for therapeutic effects. Inductively coupled plasma-optical emission spectrometer (ICP-OES) was used to quantitatively the uptake amount of  $\text{Cu}_2\text{MnS}_2$  NPs after incubation with different cells. The results demonstrated that the  $\text{Cu}_2\text{MnS}_2$  NPs could be effectively internalized by cancer cells, and the amount of cellular uptake was steadily increased with the incubation time (Figure S6). For the *in vivo* application of  $\text{Cu}_2\text{MnS}_2$  NPs, the

hemolysis assay which is a crucial toxicological factor should be investigated. As shown in Figure 3b, no hemolysis of red blood corpuscles (RBCs) was observed at tested concentrations from 0.05 to 2.0  $\text{mg mL}^{-1}$  of  $\text{Cu}_2\text{MnS}_2$  NPs, suggesting the admirable blood compatibility of  $\text{Cu}_2\text{MnS}_2$  NPs for their further *in vivo* diagnostic and therapeutic applications. Furthermore, knowledge of the clearance and biodistribution of a nanomaterial is distinctly important for its application in medical treatment. Herein, in order to study the clearance and biodistribution of  $\text{Cu}_2\text{MnS}_2$  NPs *in vivo*, S180 tumor-bearing BALB/c nude mice were injected with  $\text{Cu}_2\text{MnS}_2$  NPs through the tail vein at the dose of  $20 \text{ mg kg}^{-1}$ , then the blood of mice were collected at different time points (0.5, 1, 2, 6, 12, 24, 36 and 48 h) for blood clearance analysis. The mass of Mn was measured using an inductively coupled plasma-optical emission spectrometer (ICP-OES). The clearance of  $\text{Cu}_2\text{MnS}_2$  NPs in the blood was followed a

simple exponential decay curve with a half-decay time ( $t_{1/2}$ ) of  $\sim 15.6$  h (Figure 3c). For biodistribution studies, the mice were sacrificed, and organs were dissected, weighed, and digested after 6, 12, 24 and 48 h. The data of organ distribution and tumor uptake of  $\text{Cu}_2\text{MnS}_2$  NPs were shown in Figure 3d. It clearly showed that the liver, spleen and kidney are the main target organs. Excitingly, the tumor uptake of  $\text{Cu}_2\text{MnS}_2$  NPs was measured to be  $\sim 3.03\%$   $\text{ID g}^{-1}$  and  $\sim 6.12\%$   $\text{ID g}^{-1}$ , at 6 h and 12 h post-injection, respectively, and this value was increased to  $\sim 9.57\%$   $\text{ID g}^{-1}$  at 24 h and up to  $10.05\%$   $\text{ID g}^{-1}$  at 48 h (Figure 3d). The efficient tumor accumulation of  $\text{Cu}_2\text{MnS}_2$  NPs could be attributed to the well-known enhanced permeability and retention (EPR) effect in solid

tumors with tortuous and leaky vasculatures [55]. Therefore, the prolonged blood circulation half-decay time and high tumor accumulation of  $\text{Cu}_2\text{MnS}_2$  NPs are favorable for *in vivo* applications.

### Photothermal property of $\text{Cu}_2\text{MnS}_2$ NPs

The strong NIR-II absorption of  $\text{Cu}_2\text{MnS}_2$  NPs motivated us to explore their NIR photothermal properties. The photothermal effect of  $\text{Cu}_2\text{MnS}_2$  NPs was first studied by measuring the solution temperature changes of different concentrations of  $\text{Cu}_2\text{MnS}_2$  NPs under NIR-II laser irradiation (1064 nm,  $0.6 \text{ W cm}^{-2}$ ). As clearly shown in Figure 4a and Figure 4b, with the increase of  $\text{Cu}_2\text{MnS}_2$  NPs concentration or irradiation time, the temperature of the solutions

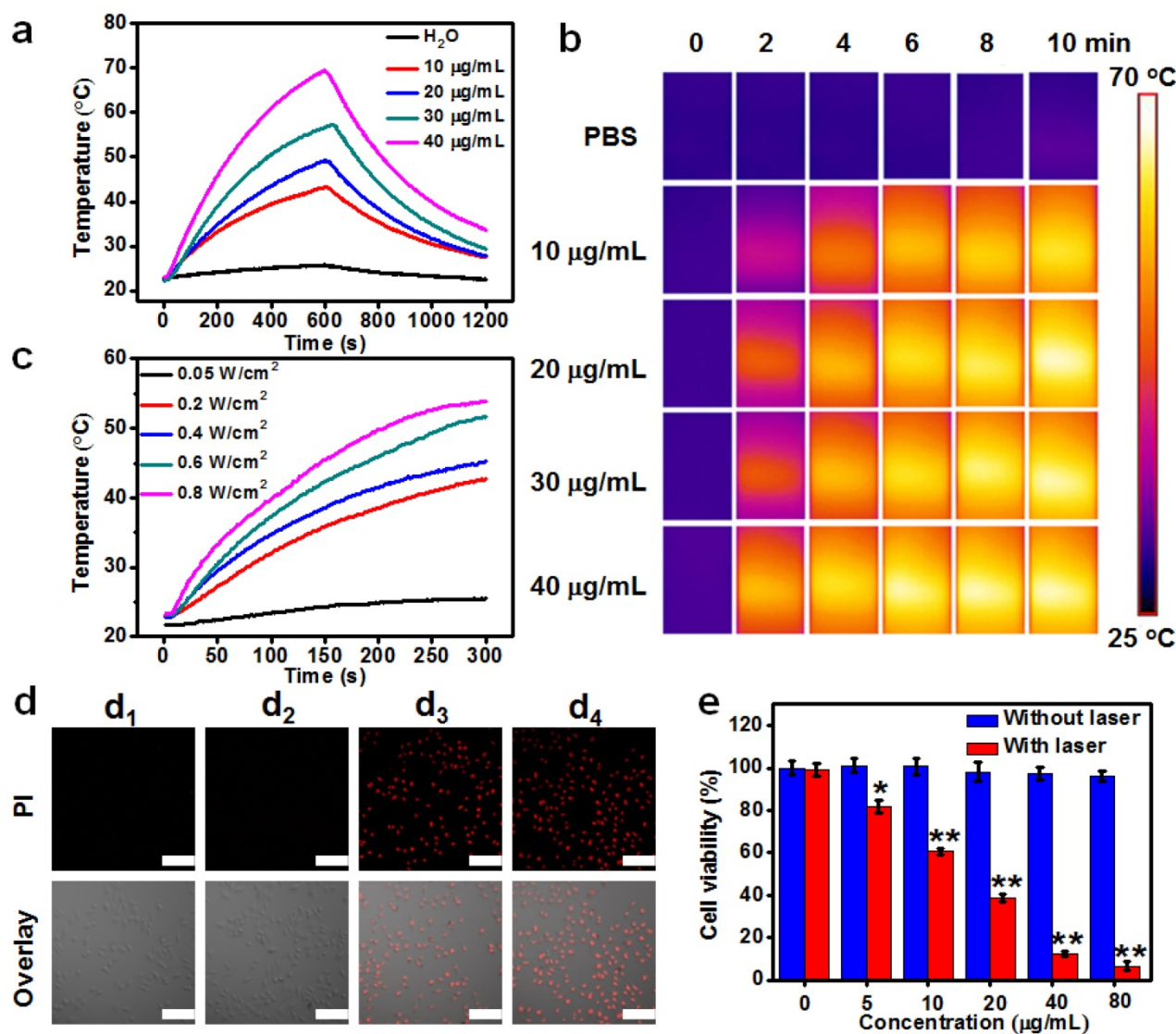


**Figure 4.** (a) Temperature elevation over a period of 10 min of exposure to a laser ( $1064 \text{ nm}$ ,  $0.6 \text{ W cm}^{-2}$ ) at various  $\text{Cu}_2\text{MnS}_2$  NPs concentrations. (b) Infrared thermal images of aqueous solutions containing different concentrations of  $\text{Cu}_2\text{MnS}_2$  NPs, captured before and after irradiation of  $1064 \text{ nm}$  laser ( $0.6 \text{ W cm}^{-2}$ ) at different time scale (0, 2, 4, 6, 8 and 10 min). (c) Photothermal heating curves of the  $\text{Cu}_2\text{MnS}_2$  NPs aqueous solution under  $1064 \text{ nm}$  laser irradiation at different power densities. (d) CLSM images of differently treated HeLa cells stained with PI. Top panels: PI fluorescence corresponding to dead cells, bottom panels: the overlay of PI fluorescence and the bright field image. (d<sub>1</sub>) 5 min laser only; (d<sub>2</sub>)  $\text{Cu}_2\text{MnS}_2$  NPs only ( $40 \mu\text{g mL}^{-1}$ ); (d<sub>3</sub>)  $\text{Cu}_2\text{MnS}_2$  NPs ( $40 \mu\text{g mL}^{-1}$ ) plus 2 min laser; (d<sub>4</sub>)  $\text{Cu}_2\text{MnS}_2$  NPs ( $40 \mu\text{g mL}^{-1}$ ) plus 5 min laser. Laser:  $1064 \text{ nm}$ ,  $0.6 \text{ W cm}^{-2}$ . All the pictures share the same scale bars:  $100 \mu\text{m}$ . (e) Cell viabilities of HeLa cells incubated to different concentrations of  $\text{Cu}_2\text{MnS}_2$  NPs with or without laser irradiation (the results are means  $\pm$  SD,  $n = 5$ , \* $p < 0.05$ , \*\* $p < 0.01$ ).

increased rapidly, while pure water or PBS showed negligible changes. Particularly, the temperature of the solution with  $30 \mu\text{g mL}^{-1}$  of  $\text{Cu}_2\text{MnS}_2$  NPs had a  $31.1 \text{ }^\circ\text{C}$  increase (from  $23.8$  to  $54.9 \text{ }^\circ\text{C}$ ) after 10 min laser irradiation at the power density of  $0.6 \text{ W cm}^{-2}$ . It has been reported that cancer cells can be killed after being kept at  $42 \text{ }^\circ\text{C}$  for 15–60 min, and the duration can be shortened to 4–6 min when the temperature is over  $50 \text{ }^\circ\text{C}$  [16, 18, 56, 57]. Thus, the temperature increase is well above the required temperature rise for efficient cancer PTT. Moreover,  $\text{Cu}_2\text{MnS}_2$  NPs displayed an obvious laser-power-dependent photothermal effect (Figure 4c). Subsequently, the molar extinction coefficient ( $\epsilon$ ) at 1064 nm for  $\text{Cu}_2\text{MnS}_2$  NPs was calculated according to Lambert-Beer law, and it was determined to be  $1.03 \times 10^{10} \text{ M}^{-1} \text{ cm}^{-1}$  (Figure S7), which was more than two orders of magnitude higher than that of Au- $\text{Cu}_9\text{S}_5$  nanostructures [14]. Furthermore, the photothermal transduction efficiency ( $\eta$ ) of  $\text{Cu}_2\text{MnS}_2$  NPs was measured according to previous method [28], and it was calculated to be  $\sim 49.38\%$  (Figure S8), which was apparently higher than that of the classical photoabsorber gold nanorods (Figure S8, AuNRs,  $\sim 26.85\%$ ) and most of the other reported PTT agents working in NIR-II window [14, 25–31]. These results demonstrated that  $\text{Cu}_2\text{MnS}_2$  NPs could convert the 1064 nm laser energy into thermal energy efficiently owing to their strong NIR-II photoabsorbance. In addition, the absorbance and photothermal performance of  $\text{Cu}_2\text{MnS}_2$  NPs solution remained almost identical even after four cycles of laser on/off (Figure S9 and S10), whereas AuNRs showed poor photothermal stability after cyclic laser irradiation (Figure S9 and Figure S10). Therefore, the demonstrated low cytotoxicity, large molar extinction coefficient, high photothermal transduction efficiency and excellent photostability of  $\text{Cu}_2\text{MnS}_2$  NPs allow them to be the promising PTT agent working in the NIR-II window.

### **In vitro NIR-II photothermal therapy**

To further verify the PTT effect, we then evaluated *in vitro* photothermal capacity of  $\text{Cu}_2\text{MnS}_2$  NPs on human cervical cancer cells (HeLa). As shown in Figure 4d, the  $\text{Cu}_2\text{MnS}_2$  NPs incubation or laser irradiation alone was unable to kill the HeLa cells. The red fluorescence (corresponding to dead cells) images demonstrated that almost all the cells were dead after incubated with  $40 \mu\text{g mL}^{-1}$  of  $\text{Cu}_2\text{MnS}_2$  NPs for 4 h and treated with 1064 nm laser irradiation ( $0.6 \text{ W cm}^{-2}$ ) for 5 min. The standard CCK-8 assays were also performed to quantitatively evaluate the photothermal cytotoxicity of  $\text{Cu}_2\text{MnS}_2$  NPs. Figure 4e showed that the viabilities of HeLa cells significantly

decreased when the cells were treated with  $\text{Cu}_2\text{MnS}_2$  NPs and laser exposure. In contrast, cells treated with the  $\text{Cu}_2\text{MnS}_2$  NPs without laser irradiation remained more than  $\sim 95\%$  viable even at a concentration of  $80 \mu\text{g mL}^{-1}$ . These *in vitro* results indicated that the combination of  $\text{Cu}_2\text{MnS}_2$  NPs and laser irradiation could kill the cancer cells effectively, thus  $\text{Cu}_2\text{MnS}_2$  NPs could act as effective NIR-II photoabsorbers for cancer PTT.

### **In vitro and in vivo MRI/MSOT dual-modal imaging**

Currently, multimodal imaging technology, especially the combination of MRI and MSOT, has attracted substantial attentions in biomedical applications towards the development of more sensitive and accurate biological imaging systems [58] and imaging-guided therapy. We herein hypothesized that the as-synthesized  $\text{Cu}_2\text{MnS}_2$  NPs might be a new suitable agent for MRI/MSOT dual-modal imaging-guided PTT owing to their strong NIR absorbance, excellent photothermal conversion effects and the presence of paramagnetic Mn ions. To investigate the capability of  $\text{Cu}_2\text{MnS}_2$  NPs as a MRI contrast agent. We first assessed the MRI performance in aqueous solutions with various concentrations of  $\text{Cu}_2\text{MnS}_2$  NPs. As shown in Figure 5a,  $T_1$ -weighted phantom images became observably brighter as the concentration of  $\text{Cu}_2\text{MnS}_2$  NPs was increased, suggesting the excellent  $T_1$  contrast ability of  $\text{Cu}_2\text{MnS}_2$  NPs. The longitudinal relaxivity ( $r_1$ ) value of  $\text{Cu}_2\text{MnS}_2$  NPs was measured to be  $4.85 \pm 0.31 \text{ mM}^{-1} \text{ s}^{-1}$  (Figure 5b), which was comparable to that of commercial contrast agent Gd-DTPA ( $3.22 \text{ mM}^{-1} \text{ s}^{-1}$ ) [39]. We further examined  $\text{Cu}_2\text{MnS}_2$  NPs as a  $T_1$ -MRI contrast agent for cancer cell imaging. Compared with the cancer cells without  $\text{Cu}_2\text{MnS}_2$  NPs incubation, brighter images were observed in  $\text{Cu}_2\text{MnS}_2$  NPs-incubated cancer cells (Figure S11). Similarly, the concentration-dependent photoacoustic (PA) signal enhancement were observed not only in solution (Figure 5c) but also in cancer cell imaging (Figure 5d) after treated with  $\text{Cu}_2\text{MnS}_2$  NPs, suggesting the potential application of  $\text{Cu}_2\text{MnS}_2$  NPs as MSOT contrast agents. Encouraged by the excellent *in vitro* MRI/MSOT performance of the  $\text{Cu}_2\text{MnS}_2$  NPs, we then evaluated the capacity of the  $\text{Cu}_2\text{MnS}_2$  NPs for *in vivo* MRI/MSOT dual-modal tumor imaging. The contrast enhancing effect *in vivo* were evaluated in S180 tumors-bearing BALB/c nude mice. The mice were anaesthetized and scanned with MRI or MSOT system before (0 h) and after (24 h) intravenous injection of  $\text{Cu}_2\text{MnS}_2$  NPs ( $20 \text{ mg kg}^{-1}$ ) solution. Firstly, the *in vivo* MRI contrast effects of  $\text{Cu}_2\text{MnS}_2$  NPs were investigated on a 3 T MRI scanner. The

tumor region showed marked positive enhancement (brighter signal) after injection, indicating that  $\text{Cu}_2\text{MnS}_2$  NPs can produce strong  $T_1$  contrast enhancements in the tumor (Figure 5e). To quantify the contrast enhancement, the signal-to-noise ratio (SNR) for MRI was calculated [52]. Compared to before injection, the SNR value of tumor region after injection had a 6.43-fold enhancement (Figure 5f), further demonstrating that  $\text{Cu}_2\text{MnS}_2$  NPs can shorten  $T_1$  relaxation time of tumor. We then examined the *in vivo* PA contrast effects of  $\text{Cu}_2\text{MnS}_2$  NPs using a

MSOT system. The PA signals in the tumor region were remarkably enhanced after injection with  $\text{Cu}_2\text{MnS}_2$  NPs (Figure 5g), with the PA intensity having a 6.85-fold increase (Figure 5h) at 24 h of post injection under irradiation of a 900 nm laser source, confirming the feasibility of  $\text{Cu}_2\text{MnS}_2$  NPs for *in vivo* MSOT contrast enhancement. The excellent *in vitro* and *in vivo* MRI/MSOT dual-modal imaging capabilities of  $\text{Cu}_2\text{MnS}_2$  NPs made them as promising nanomaterials for cancer diagnosis, which could be further applied in imaging-guided PTT.

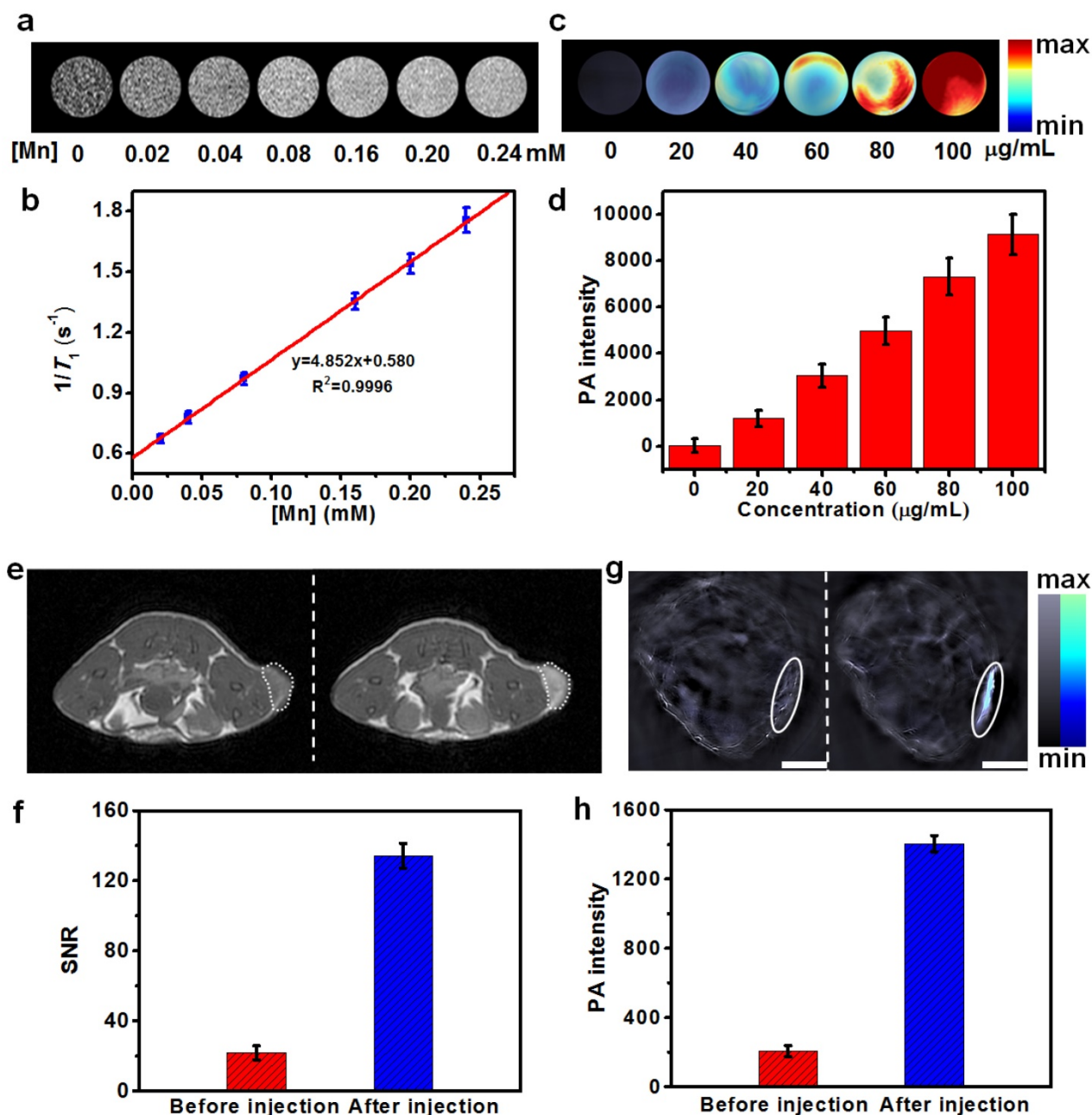


**Figure 5.** (a)  $T_1$ -weighted phantom images of  $\text{Cu}_2\text{MnS}_2$  NPs with different [Mn] concentrations at 0.5 T. (b) The linear fitting of longitudinal relaxation rates at 0.5 T versus [Mn] concentrations for  $\text{Cu}_2\text{MnS}_2$  NPs. The  $r_1$  of  $\text{Cu}_2\text{MnS}_2$  NPs was determined to be  $4.85 \pm 0.31 \text{ mM}^{-1} \text{ s}^{-1}$  ( $n = 3$ ). (c) Photoacoustic (PA) images and (d) corresponding PA intensities of  $\text{Cu}_2\text{MnS}_2$  NPs solutions with different concentrations. (e) *In vivo*  $T_1$ -weighted MRI images and (f) corresponding quantification of the signal-to-noise ratios (SNR), and (g) *in vivo* MSOT images (Scale bars: 3 mm) and (h) corresponding quantification of intensities of mice tumor region before and after the injection of  $\text{Cu}_2\text{MnS}_2$  NPs ( $20 \text{ mg kg}^{-1}$ ), respectively.

## Deep tissue photothermal therapy in NIR-II window

Because of its low scattering and energy absorption of tissue transmission, NIR-II light displays more deeply tissue penetration depths than NIR-I light [15]. Deep tissue photothermal effect of the as-synthesized  $\text{Cu}_2\text{MnS}_2$  NPs in the NIR-II window were investigated by using different thicknesses of pork tissues as model biological tissues (Figure S12a). During the laser irradiation process (1064 or 808 nm,  $1 \text{ W cm}^{-2}$ ), a thermal imaging camera was used to record the temperature changes of  $\text{Cu}_2\text{MnS}_2$  NPs solution with or without cover of pork tissues (Figure S12b, c). Moreover, the obtained temperature changes under different thicknesses of pork tissues were normalized to the maximum temperature increase which measured the  $\text{Cu}_2\text{MnS}_2$  NPs solution without tissue cover. The results were plotted as functions of tissue thicknesses and fitted with exponential decay curves. As shown in Figure S13, the relative rate of temperature changes under different pork tissue thicknesses exposed to 808 nm laser was obviously faster than that of under 1064 nm laser irradiation, confirming that the as-synthesized  $\text{Cu}_2\text{MnS}_2$  NPs have great potential for deep tissue PTT in the NIR-II window.

## In vivo photothermal therapy in NIR-II window and long-term toxicity study of $\text{Cu}_2\text{MnS}_2$ NPs

The feasibility of using  $\text{Cu}_2\text{MnS}_2$  NPs for *in vivo* imaging-guided NIR-II PTT was investigated. The *in vivo* photothermal effect of  $\text{Cu}_2\text{MnS}_2$  NPs was first measured by using an IR thermal camera to monitor the temperature changes of the tumor areas. IR thermographic images showed that the temperature at the tumor region can rapidly increase from  $\sim 33^\circ\text{C}$  to  $\sim 55^\circ\text{C}$  after intravenous injection of  $\text{Cu}_2\text{MnS}_2$  NPs ( $20 \text{ mg kg}^{-1}$ ) under 1064 nm laser irradiation ( $0.6 \text{ W cm}^{-2}$ ) within 3 min (Figure 6a,b), which was capable of inducing sufficient local hyperthermia to kill tumor cells. In the control test, the temperature of the tumors region that injected with PBS increased only  $\sim 3^\circ\text{C}$  during the whole irradiation process (Figure 6a,b). To further verify the photothermal therapeutic effect of  $\text{Cu}_2\text{MnS}_2$  NPs, the S180 tumor-bearing mice were randomly divided into four groups ( $n = 5$  for each group) for different treatment processes: without any treatment (control group), intravenous injected with 200  $\mu\text{L}$  of PBS and then irradiated with 1064 nm laser ( $0.6 \text{ W cm}^{-2}$ ) for 10 min (PBS + laser group), intravenous injected with 200  $\mu\text{L}$  of  $20 \text{ mg kg}^{-1}$   $\text{Cu}_2\text{MnS}_2$  NPs only ( $\text{Cu}_2\text{MnS}_2$  NPs group), and intravenous injected with 200  $\mu\text{L}$  of  $20 \text{ mg kg}^{-1}$   $\text{Cu}_2\text{MnS}_2$  NPs and then irradiated with 1064 nm laser ( $0.6 \text{ W cm}^{-2}$ ) for 10 min ( $\text{Cu}_2\text{MnS}_2$  NPs + laser group). The tumor volume and weight of mice were measured

every other day after the treatments described above. As shown in Figure 6c and Figure 6d, in  $\text{Cu}_2\text{MnS}_2$  NPs + laser group, the tumors were successfully eliminated without any reoccurrence. In striking contrast, the mice in the other three groups showed rapid tumors growth within 28 days (Figure 6c,d), suggesting that neither laser irradiation alone nor  $\text{Cu}_2\text{MnS}_2$  NPs injection alone could suppresses the tumors growth. Meanwhile, the body weight of mice in  $\text{Cu}_2\text{MnS}_2$  NPs + laser group was gradually increased, indicating the recovery of the mice after the PTT treatment, while the mice in other three groups were in poor health with weight loss because of the rapid growth of malignant tumors (Figure S14). Furthermore, the mice in  $\text{Cu}_2\text{MnS}_2$  NPs + laser group could survive over 57 days and only one mouse dead at day of 57, while mice in the other three groups showed an average life time of less than 37 days (Figure 6e). Moreover, hematoxylin and eosin (H&E) staining of tumor slices revealed that the tumor cells in  $\text{Cu}_2\text{MnS}_2$  NPs + laser group were severely destroyed (necrosis with cells deformation) due to the PTT treatment. However, tumor cells in the other three groups retained regular cell morphology with intact cell nucleus (Figure 6f). In addition, no obvious noticeable organ damage or adverse effect associated with the administration of the  $\text{Cu}_2\text{MnS}_2$  NPs was observed at the tested dose ( $20 \text{ mg kg}^{-1}$ ) (Figure S15), indicating the safety of  $\text{Cu}_2\text{MnS}_2$  NPs *in vivo*. Furthermore, to investigate the detailed long-term toxicity of  $\text{Cu}_2\text{MnS}_2$  NPs, hematology analysis and blood biochemical assays were carried out for healthy mice after intravenous injection of  $\text{Cu}_2\text{MnS}_2$  NPs ( $20 \text{ mg kg}^{-1}$ ), at the 1st, 7th, 14th, and 28th day post-injection (Figure S16 and Figure S17). Neither deaths nor serious body weight loss was observed in all test groups during the study period. Encouragingly, all of measured parameters (including routine blood parameters and serum biochemistry parameters) in  $\text{Cu}_2\text{MnS}_2$  NPs injected groups were in normal reference ranges [59], and showed no significant physiological difference compared to the control groups (Figure S16 and Figure S17). In addition, the long-term *in vivo* biodistribution of Mn amounts in different organs (including the heart, liver, spleen, lung, kidney, tumor, intestine, stomach, brain and muscle) were also carried out. As shown in Figure S18, the amounts of Mn in all organs were decreased at 7th day, and were reached to very low levels at 28th day, implying that the  $\text{Cu}_2\text{MnS}_2$  NPs could be excreted out of these organs, thus avoiding the potential adverse or side effects of the organs. These results clearly demonstrated that  $\text{Cu}_2\text{MnS}_2$  NPs could be a promising agent for tumor NIR-II PTT *in vivo*.

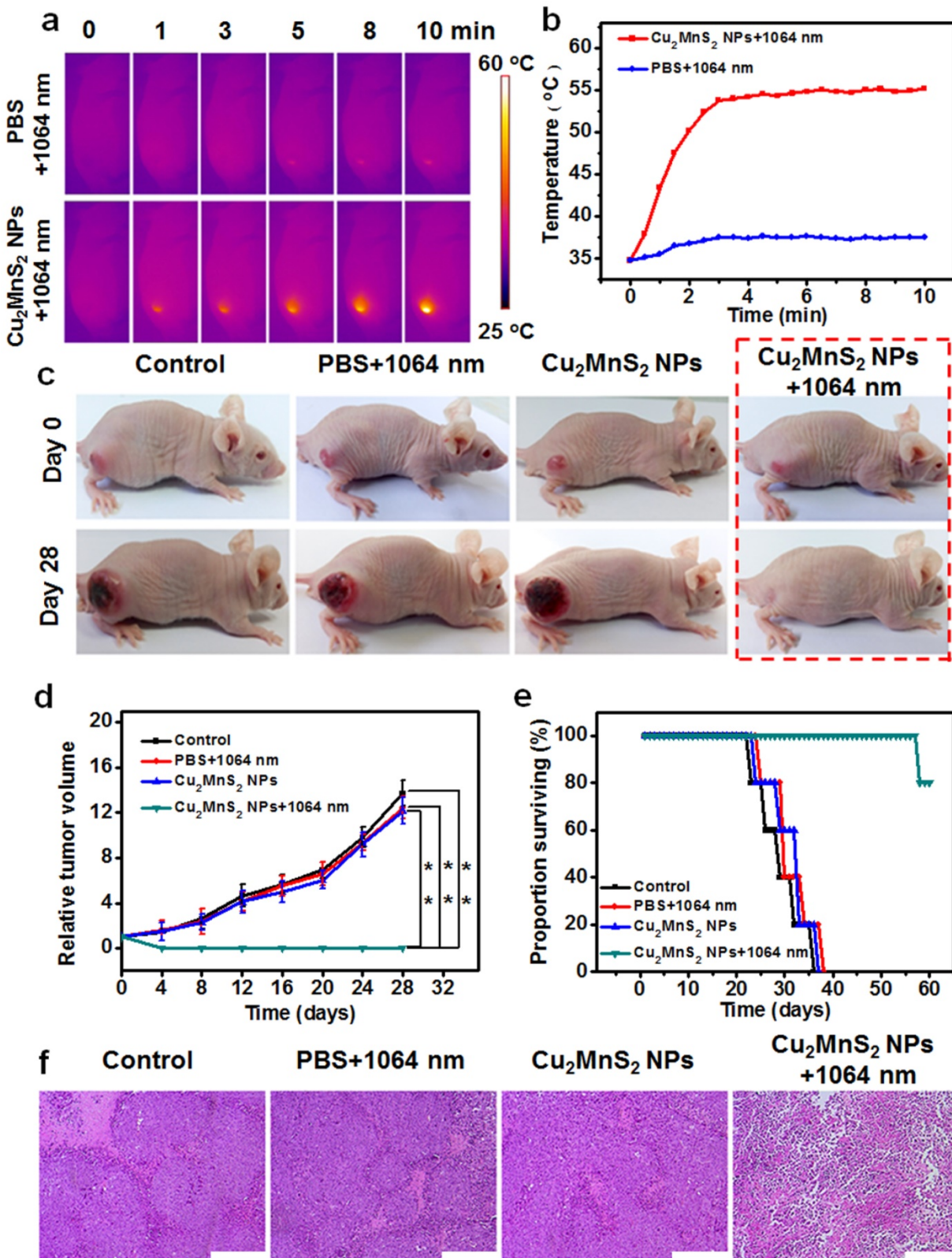


**Figure 6.** (a) IR thermal images of tumor-bearing mice with intravenous injection of PBS or  $\text{Cu}_2\text{MnS}_2$  NPs under 1064 nm laser irradiation (24 h of post-injection) ( $0.6 \text{ W cm}^{-2}$ ) for different times. (b) Tumor temperatures of mice monitored by the IR thermal camera as a function of the irradiation time. (c) Representative photos of mice in different groups before and after treatment. (d) Tumor growth curves of tumor-bearing mice in different groups after treatment (the results are means  $\pm$  SD,  $n = 5$  for each group, \* $p < 0.05$ , \*\* $p < 0.01$ ). (e) Surviving proportion of four different groups after various treatments ( $n = 5$  for each group). (f) H&E-stained images of tumor sections collected from mice of different groups after various treatments. Scale bars are 200  $\mu\text{m}$ .

## Conclusions

In summary, we have, for the first time, developed a new 2D nanoplatform based on  $\text{Cu}_2\text{MnS}_2$  NPs for MRI/MSOT dual-modal imaging-guided PTT of cancer in the NIR-II window. The  $\text{Cu}_2\text{MnS}_2$  NPs contain a variety of remarkable properties. First, the synthesis of  $\text{Cu}_2\text{MnS}_2$  NPs is easy to achieve via a one-pot and facile solvothermal method. Second, the  $\text{Cu}_2\text{MnS}_2$  NPs possesses excellent colloidal stability and biocompatibility. Third, with strong NIR-I and NIR-II absorption, large molar extinction coefficient ( $\epsilon$ ), high photothermal conversion efficiency ( $\eta$ ) and outstanding photostability as well as enhanced  $T_1$ -shortening effect, the  $\text{Cu}_2\text{MnS}_2$  NPs can serve as effective agents for MRI/MSOT (900 nm laser source) dual-modal imaging-guided cancer PTT *in vitro* and *in vivo* in the NIR-II window. Overall, taking advantage of the inspiring features of the  $\text{Cu}_2\text{MnS}_2$  NPs, we might provide a new perspective for exploring new 2D-based nanoplatforms with improved properties for the biomedical application.

## Materials and Methods

### Chemicals and Materials

Copper (II) chloride dihydrate ( $\text{CuCl}_2 \cdot 2\text{H}_2\text{O}$ ,  $\geq 99\%$ ), Manganese (II) chloride tetrahydrate ( $\text{MnCl}_2 \cdot 4\text{H}_2\text{O}$ ,  $\geq 98\%$ ), anhydrous sodium sulfide ( $\text{Na}_2\text{S}$ ,  $\geq 98\%$ ) and monomethoxycarboxyl polyethylene glycol (mPEG-COOH, MW=2000, AR) were purchased from Sigma-Aldrich. Cell Counting Kit-8 (CCK-8) was purchased from Dojindo (Japan). All other reagents with analytical reagent grade were purchased from Sinopharm Chemical Reagent Co., Ltd. (China), and were used without further purification. The ultrapure water used in all experiments was obtained from a Millipore water purification system (resistivity 18.2  $\text{M}\Omega \cdot \text{cm}$ ).

### Animal Models

All the animal experiments were executed according to the protocol approved by the Institutional Animal Care and Use Committee of Fujian Medical University.

### Preparation of $\text{Cu}_2\text{MnS}_2$ NPs

In order to synthesis the desired  $\text{Cu}_2\text{MnS}_2$  NPs, a series of experiments were carried out. The synthetic strategy is based on a one-pot solvothermal method involving mPEG-COOH,  $\text{CuCl}_2 \cdot 2\text{H}_2\text{O}$ ,  $\text{MnCl}_2 \cdot 4\text{H}_2\text{O}$  and  $\text{Na}_2\text{S}$  (different proportion of Cu:Mn:S, molar ratio): (1) The reactions were under the same conditions but with different proportion of Cu:Mn:S (100 mg of mPEG-COOH, reaction temperature: 120 °C, reaction time: 6 h); (2) The reactions were under

the same conditions but with different amounts of mPEG-COOH (Cu:Mn:S = 1:1:3, reaction temperature: 120 °C, reaction time: 6 h); (3) The reactions were under the same conditions but with different reaction time (Cu:Mn:S = 1:1:3, 100 mg of mPEG-COOH, reaction temperature: 120 °C); and (4) The reactions were under the same conditions but with different reaction temperature (Cu:Mn:S = 1:1:3, 100 mg of mPEG-COOH, reaction time: 6 h). Plate-like products with well-defined uniform morphology can be obtained under certain reaction conditions: Cu:Mn:S = 1:1:3, 100 mg of mPEG-COOH, reaction temperature: 120 °C, reaction time: 6 h. The detail procedures are as follows:  $\text{CuCl}_2 \cdot 2\text{H}_2\text{O}$  (0.1705 g, 1 mmol),  $\text{MnCl}_2 \cdot 4\text{H}_2\text{O}$  (0.1258 g, 1mmol) and mPEG-COOH (0.1000 g) was first dissolved in 20 mL ethylene glycol (EG) sufficiently. Then, another 20 mL of EG containing  $\text{Na}_2\text{S}$  (0.2340 g, 3 mmol) was slowly added into the above solution with vigorous magnetic stirring. After stirring for 2 h to form a dark brown turbid solution, the resulting solution was transferred to a stainless steel autoclave (50 mL), and heated at 120 °C for 6 h. After being cooled to room temperature, the green-dark precipitate was collected by centrifugation and washed with ethanol and deionized water two times, respectively, and finally redispersed in water. The obtained solution was stored in darkness at 4 °C for further use.

### UV-vis-NIR Absorption Spectrum Measurements

To investigate the absorption of  $\text{Cu}_2\text{MnS}_2$  NPs, 1 mL of  $\text{Cu}_2\text{MnS}_2$  NPs aqueous solution with different concentrations were first prepared. Then, the UV-vis-NIR absorption spectra of  $\text{Cu}_2\text{MnS}_2$  NPs were collected by an UH4150 Spectrophotometer (Hitachi Co., Ltd., Japan) in the range of 500-1500 nm.

### Measurement of the Photothermal Performance

The photothermal performance of  $\text{Cu}_2\text{MnS}_2$  NPs was investigated by recording the temperature changes of the solution under continuous laser irradiation. In a typical experiment, 1 mL aqueous solutions of  $\text{Cu}_2\text{MnS}_2$  NPs with different concentrations were irradiated by 1064 nm (0.6  $\text{W cm}^{-2}$ ) lasers for 10 min. The temperature changes were monitored by a digital thermometer during the irradiation period.

### In Vitro Photothermal Therapy

HeLa cells were incubated with or without  $\text{Cu}_2\text{MnS}_2$  NPs (40  $\mu\text{g mL}^{-1}$ ) for 4 h and then exposed to a 1064 nm (0.6  $\text{W cm}^{-2}$ ) laser for 5 min. After staining with propidium iodide (PI) for 30 min, the cells were

imaged by a confocal laser scanning microscope (Nikon C2, Japan) to capture the red fluorescence of dead cells.

To quantitatively evaluate the photothermal cytotoxicity of  $\text{Cu}_2\text{MnS}_2$  NPs, HeLa cells were incubated in 96-well plates (100  $\mu\text{L}$ ,  $1 \times 10^4$  cells per well) at 37 °C in a humidified atmosphere containing 5%  $\text{CO}_2$  for 24 h. The  $\text{Cu}_2\text{MnS}_2$  NPs with different concentrations were added and the cells were further incubated for 4 h. After with or without irradiated by a 1064 nm (0.6  $\text{W cm}^{-2}$ ) laser for 5 min, the cells were allowed to incubate for another 24 h. The standard CCK-8 assays were carried out to evaluate the cell viabilities.

### Measurement of MRI Relaxation Properties and Cellular MRI

To measure the  $T_1$  relaxation properties,  $\text{Cu}_2\text{MnS}_2$  NPs with different [Mn] concentrations were prepared and measured using a 0.5 T NMI20-Analyst NMR system (Niumag Corporation, Shanghai, China). The longitudinal relaxation times ( $T_1$ ) were measured using an inversion recovery (IR) sequence. The longitudinal relaxivity ( $r_1$ ) was determined from the slope of  $1/T_1$  values as the function of [Mn] concentrations. For cellular MRI, S180 cells with a density of  $1 \times 10^5$  cells/well were seeded in a 6-well tissue culture plate and incubated for 24 h. Then, the medium was replaced with fresh RPMI-1640 medium containing different concentrations of  $\text{Cu}_2\text{MnS}_2$  NPs and cultured for different time. After removing the cell culture medium, cells were immobilized and gently washed with PBS buffer for five times, then the cells were resuspended and MRI scanning were carried out to collect the signals.  $T_1$ -weighted MR images were acquired using a 2D multi-slice spin-echo (MSE) sequence with the following parameters: TR/TE = 100/2 ms,  $512 \times 512$  matrices, slices = 1, thickness = 1 mm, and NS = 4.

### In Vivo MRI

Tumor-bearing mice were prepared by subcutaneously injecting a suspension of  $2 \times 10^6$  S180 cells into the back of the hind leg. MRI scanning was first performed before  $\text{Cu}_2\text{MnS}_2$  NPs injection as the control. Next, the mice were intravenously injected with  $\text{Cu}_2\text{MnS}_2$  NPs (20  $\text{mg kg}^{-1}$ ).  $T_1$ -weighted images of the mice were collected on a 3 T MRI scanner after 24 h of post-injection (GE Discovery MR750). All the images were obtained using an FSE sequence under the following parameters: TR/TE = 513/14.5 ms, FOV =  $8 \times 8$  cm,  $320 \times 224$  matrices, thickness = 1 mm. To quantify the contrast enhancement, the signal-to-noise

ratio (SNR) was measured by finely analyzing regions of interest (ROIs) of the images of tumor sites [52].

### In Vitro and In Vivo MSOT

Different concentrations of  $\text{Cu}_2\text{MnS}_2$  NPs solutions (0, 20, 40, 60, 80, 100  $\mu\text{g mL}^{-1}$ ) were loaded into agar gel cylinders. The *in vitro* MSOT was carried out on the InVision 128 MSOT system (iThera Medical, Germany) to collect the optoacoustic signals (laser wavelengths: 680-980 nm, the main experimental parameters were 5 nm wavelengths for each slice). After the reconstruction (900 nm) of the obtained MSOT images, MSOT signals were calculated by finely analyzing regions of interest (ROIs) of the images of tumor sites. The cellular MSOT experiment processes were similar with the cellular MRI (see cellular MRI).

For *in vivo* MSOT, MSOT scanning was first performed before  $\text{Cu}_2\text{MnS}_2$  NPs injection as controls. Next, the mice were intravenously injected with  $\text{Cu}_2\text{MnS}_2$  NPs (20  $\text{mg kg}^{-1}$ ). After 24 h of post-injection, the mice were scanned from 680 nm to 980 nm with the MSOT (MSOT InVision 128, iThera medical, Germany) to collect signals. The main experimental parameters were 5 nm wavelengths for each slice, with the region of interest being 25 mm. A water heating system was used to maintain the body temperature of the mice to  $\sim 37$  °C during the scanning processes.

### In Vivo PTT

The mice were divided into four groups with five mice per group when the tumor size reached about 80  $\text{mm}^3$ . In one group, the mice were intravenously injected with  $\text{Cu}_2\text{MnS}_2$  NPs (20  $\text{mg kg}^{-1}$ ). After the 24 h of post-injections, tumors were irradiated with or without NIR-II laser 1064 nm (0.6  $\text{W cm}^{-2}$ ) for 10 min. The other three groups are: mice without any treatment (control group), mice were only intravenously injected with  $\text{Cu}_2\text{MnS}_2$  NPs ( $\text{Cu}_2\text{MnS}_2$  NPs only group), and mice intravenous injected with PBS and then irradiated with laser (PBS + laser group). Infrared thermal imaging system was performed for studying the *in vivo* photothermal effect of  $\text{Cu}_2\text{MnS}_2$  NPs. IR thermographs was recorded by a FLIR Ax5 infrared camera. The tumor sizes were measured by a digital caliper every other day. The tumor volumes were calculated through the equation: volume =  $ab^2/2$ , in which a is the maximum diameter and b is the minimum diameter of tumor, respectively. Relative tumor volumes were calculated as  $V/V_0$ , where  $V_0$  is the tumor volume when the treatment was initiated.

## Hematology Analysis, Blood Biochemical Assay and Histology Analysis

For hematology and biochemical analysis, the blood was collected from mice and separated by centrifugation into cellular and serum fractions. The hematology data and serum biochemistry data were recorded on MINDRAY BC-5500 automated hematology analyzer (MINDRAY, China) and HITACHI 7020 automatic biochemical analyzer (HITACHI, Japan), respectively. For histology analysis, mice were sacrificed and major organs from those mice were harvested, dipped in 10% neutral buffered formalin, then embedded in paraffin, stained with H&E and pathology were examined by a digital microscope. All the statistics were based on standard deviations of 5 mice per group.

## Abbreviations

2D: two-dimensional; MRI: magnetic resonance imaging; MSOT: multispectral optoacoustic tomography; PTT: photothermal therapy; Cu<sub>2</sub>MnS<sub>2</sub> NPs: Cu<sub>2</sub>MnS<sub>2</sub> nanoplates; MPE: maximum permissible exposure; NIR: near-infrared; NIR-I: the first biological window; NIR-II: the second biological window; EG: ethylene glycol; mPEG-COOH: monomethoxycarboxyl polyethylene glycol; TEM: transmission electron microscope; DLS: dynamic light scattering; AFM: atomic force microscopy; EDS: energy dispersive X-ray spectroscopy; XRD: X-ray powder diffraction; XPS: X-ray photoelectron spectroscopy; FTIR: fourier-transform infrared spectroscopy; TGA: thermogravimetric analysis; ICP-OES: inductively coupled plasma-optical emission spectrometer; UV-vis: ultraviolet-visible; CCK-8: cell counting kit-8; MCF-7: human breast-cancer cells; HeLa: human cervical cancer cells; S180: murine sarcoma cancer cells; AuNRs: gold nanorods; PI: pyridinium iodide; PA: photoacoustic; T<sub>1</sub>: longitudinal relaxation times; τ<sub>1</sub>: longitudinal relaxivity; i.v. injection: intravenous injection.

## Supplementary Material

Additional detailed experimental section, characterization and results: Cell Culture, Cellular Uptake of Cu<sub>2</sub>MnS<sub>2</sub> NPs and Cytotoxicity Assay; Hemolysis Assay; Biodistribution; Calculation of the Photothermal Conversion Efficiency; Supplementary Figures S1-S18.

<http://www.thno.org/v07p4763s1.pdf>

## Acknowledgements

This research was supported by the National Natural Science Foundation of China (Nos. 21475026,

U1505221, 21635002, 81501461, 21775025), Natural Science Foundation of Fujian Province of China (Nos. 2015H6011, 2017J05131, 2017J01199), the Program for Changjiang Scholars and Innovative Research Team in University (No. IRT15R11), and the Independent Research Project of State Key Laboratory of Photocatalysis on Energy and Environment (No. 2014B02).

## Competing Interests

The authors have declared that no competing interest exists.

## References

- Lim EK, Kim T, Paik S, Haam S, Huh YM, Lee K. Nanomaterials for Theranostics: Recent Advances and Future Challenges. *Chem Rev.* 2015; 115: 327-94.
- Vivero-Escoto JL, Slowing II, Wu CW, Lin VSY. Photoinduced Intracellular Controlled Release Drug Delivery in Human Cells by Gold-Capped Mesoporous Silica Nanosphere. *J Am Chem Soc.* 2009; 131: 3462-3.
- Lal S, Clare SE, Halas NJ. Nanoshell-Enabled Photothermal Cancer Therapy: Impending Clinical Impact. *Acc Chem Res.* 2008; 41: 1842-51.
- Chen GY, Roy I, Yang CH, Prasad PN. Nanochemistry and Nanomedicine for Nanoparticle-based Diagnostics and Therapy. *Chem Rev.* 2016; 116: 2826-85.
- Cheng L, Wang C, Feng LZ, Yang K, Liu Z. Functional Nanomaterials for Phototherapies of Cancer. *Chem Rev.* 2014; 114: 10869-939.
- Melancon MP, Zhou M, Li C. Cancer Theranostics With Near-Infrared Light-Activatable Multimodal Nanoparticles. *Acc Chem Res.* 2011; 44: 947-56.
- Zedan AF, Moussa S, Terner J, Atkinson G, El-Shall MS. Ultrasmall Gold Nanoparticles Anchored to Graphene and Enhanced Photothermal Effects by Laser Irradiation of Gold Nanostructures in Graphene Oxide Solutions. *ACS Nano.* 2013; 7: 627-36.
- Yuan H, Fales AM, Vo-Dinh T. TAT Peptide-Functionalized Gold Nanostars: Enhanced Intracellular Delivery and Efficient NIR Photothermal Therapy Using Ultralow Irradiance. *J Am Chem Soc.* 2012; 134: 11358-61.
- Li M, Yang XJ, Ren JS, Qu KG, Qu XG. Using Graphene Oxide High Near-Infrared Absorbance for Photothermal Treatment of Alzheimer's Disease. *Adv Mater.* 2012; 24: 1722-8.
- Maestro LM, Haro-Gonzalez P, del Rosal B, Ramiro J, Caamano AJ, Carrasco E, et al. Heating Efficiency of Multi-Walled Carbon Nanotubes in the First and Second Biological Windows. *Nanoscale.* 2013; 5: 7882-9.
- Weissleder R, Tung CH, Mahmood U, Bogdanov A. In Vivo Imaging of Tumors with Protease-Activated Near-Infrared Fluorescent Probes. *Nat Biotechnol.* 1999; 17: 375-8.
- Wu S, Butt HJ. Near-Infrared-Sensitive Materials Based on Upconverting Nanoparticles. *Adv Mater.* 2016; 28: 1208-26.
- Prodi L, Rampazzo E, Rastrelli F, Speghini A, Zaccheroni N. Imaging Agents Based on Lanthanide Doped Nanoparticles. *Chem Soc Rev.* 2015; 44: 4922-52.
- Ding XG, Liow CH, Zhang MX, Huang RJ, Li CY, Shen H, et al. Surface Plasmon Resonance Enhanced Light Absorption and Photothermal Therapy in the Second Near-Infrared Window. *J Am Chem Soc.* 2014; 136: 15684-93.
- Bashkatov AN, Genina EA, Kochubey VI, Tuchin VV. Optical Properties of Human Skin, Subcutaneous and Mucous Tissues in the Wavelength Range From 400 to 2000 nm. *J Phys D: Appl Phys.* 2005; 38: 2543-55.
- Ke KM, Lin LS, Liang H, Chen X, Han C, Li J, et al. Polypyrrole Nanoprobes with Low Non-Specific Protein Adsorption for Intracellular mRNA Detection and Photothermal Therapy. *Chem Commun.* 2015; 51: 6800-3.
- Song JB, Wang F, Yang XY, Ning B, Harp MG, Culp SH, et al. Gold Nanoparticle Coated Carbon Nanotube Ring with Enhanced Raman Scattering and Photothermal Conversion Property for Theranostic Applications. *J Am Chem Soc.* 2016; 138: 7005-15.
- Lin LS, Cong ZX, Cao JB, Ke KM, Peng QL, Gao JH, et al. Multifunctional Fe<sub>3</sub>O<sub>4</sub>/Polydopamine Core-Shell Nanocomposites for Intracellular mRNA Detection and Imaging-Guided Photothermal Therapy. *ACS Nano.* 2014; 8: 3876-83.
- Li B, Ye KC, Zhang YX, Qin JB, Zou RJ, Xu KB, et al. Photothermal Theragnosis Synergistic Therapy Based on Bimetal Sulphide Nanocrystals Rather Than Nanocomposites. *Adv Mater.* 2015; 27: 1339-45.
- Li J, Jiang F, Yang B, Song XR, Liu Y, Yang HH, et al. Topological Insulator Bismuth Selenide as a Theranostic Platform for Simultaneous Cancer Imaging and Therapy. *Sci Rep-Uk.* 2013; 3.
- Ke HT, Wang JR, Dai ZF, Jin YS, Qu EZ, Xing ZW, et al. Gold-Nanoshelled Microcapsules: A Theranostic Agent for Ultrasound Contrast Imaging and Photothermal Therapy. *Angew Chem Int Ed.* 2011; 50: 3017-21.
- Hong GS, Lee JC, Robinson JT, Raaz U, Xie LM, Huang NF, et al. Multifunctional in Vivo Vascular Imaging Using Near-Infrared II Fluorescence. *Nat Med.* 2012; 18: 1841-6.

23. Ruddy DA, Johnson JC, Smith ER, Neale NR. Size and Bandgap Control in the Solution-Phase Synthesis of Near-Infrared-Emitting Germanium Nanocrystals. *ACS Nano*. 2010; 4: 7459-66.
24. Hong GS, Robinson JT, Zhang YJ, Diao S, Antaris AL, Wang QB, et al. In Vivo Fluorescence Imaging with Ag<sub>2</sub>S Quantum Dots in the Second Near-Infrared Region. *Angew Chem Int Ed*. 2012; 51: 9818-21.
25. Tsai MF, Chang SHG, Cheng FY, Shanmugam V, Cheng YS, Su CH, et al. Au Nanorod Design as Light-Absorber in the First and Second Biological Near-Infrared Windows for in Vivo Photothermal Therapy. *ACS Nano*. 2013; 7: 5330-42.
26. Li A, Li X, Yu XJ, Li W, Zhao RY, An X, et al. Synergistic Thermoradiotherapy Based on PEGylated Cu<sub>2</sub>BiS<sub>3</sub> Ternary Semiconductor Nanorods with Strong Absorption in the Second Near-Infrared Window. *Biomaterials*. 2017; 112: 164-75.
27. Wu ZC, Li WP, Luo CH, Su CH, Yeh CS. Rattle-Type Fe<sub>3</sub>O<sub>4</sub>@CuS Developed to Conduct Magnetically Guided Photoinduced Hyperthermia at First and Second NIR Biological Windows. *Adv Funct Mater*. 2015; 25: 6527-37.
28. Guo CS, Yu HJ, Feng B, Gao WD, Yan M, Zhang ZW, et al. Highly Efficient Ablation of Metastatic Breast Cancer Using Ammonium-Tungsten-Bronze Nanocube as a Novel 1064 nm-Laser-Driven Photothermal Agent. *Biomaterials*. 2015; 52: 407-16.
29. Vijayaraghavan P, Liu CH, Vankayala R, Chiang CS, Hwang KC. Designing Multi-Branched Gold Nanochinins for NIR Light Activated Dual Modal Photodynamic and Photothermal Therapy in the Second Biological Window. *Adv Mater*. 2014; 26: 6689-95.
30. Ji MW, Xu M, Zhang W, Yang ZZ, Huang L, Liu JJ, et al. Structurally Well-Defined Au@Cu<sub>2</sub>S Core-Shell Nanocrystals for Improved Cancer Treatment Based on Enhanced Photothermal Efficiency. *Adv Mater*. 2016; 28: 3094-101.
31. Guo W, Guo CS, Zheng NN, Sun TD, Liu SQ. Cs<sub>2</sub>WO<sub>6</sub> Nanorods Coated with Polyelectrolyte Multilayers as a Multifunctional Nanomaterial for Bimodal Imaging-Guided Photothermal/Photodynamic Cancer Treatment. *Adv Mater*. 2017; DOI: 10.1002/adma.201604157.
32. Lee DE, Koo H, Sun IC, Ryu JH, Kim K, Kwon IC. Multifunctional Nanoparticles for Multimodal Imaging and Theragnosis. *Chem Soc Rev*. 2012; 41: 2656-72.
33. Rooney W. MRI: From Picture to Proton. *Health Phys*. 2003; 85: 504-5.
34. Weissleder R, Pittet MJ. Imaging in the Era of Molecular Oncology. *Nature*. 2008; 452: 580-9.
35. Nguyen KT, Zhao Y. Engineered Hybrid Nanoparticles for On-Demand Diagnostics and Therapeutics. *Acc Chem Res*. 2015; 48: 3016-25.
36. Wang LHV, Hu S. Photoacoustic Tomography: In Vivo Imaging from Organelles to Organs. *Science*. 2012; 335: 1458-62.
37. Ntziachristos V, Razansky D. Molecular Imaging by Means of Multispectral Photoacoustic Tomography (MSOT). *Chem Rev*. 2010; 110: 2783-94.
38. Lin LS, Yang X, Zhou Z, Yang Z, Jacobson O, Liu Y, et al. Yolk-Shell Nanostructure: An Ideal Architecture to Achieve Harmonious Integration of Magnetic-Plasmonic Hybrid Theranostic Platform. *Adv Mater*. 2017; DOI: 10.1002/adma.201606681.
39. Yang WT, Guo WS, Le WJ, Lv GX, Zhang FH, Shi L, et al. Albumin-Bioinspired Gd:CuS Nanotheranostic Agent for In Vivo Photoacoustic/Magnetic Resonance Imaging-Guided Tumor-Targeted Photothermal Therapy. *ACS Nano*. 2016; 10: 10245-57.
40. Pu KY, Shuhendler AJ, Jokerst JV, Mei JG, Gambhir SS, Bao ZN, et al. Semiconducting Polymer Nanoparticles as Photoacoustic Molecular Imaging Probes in Living Mice. *Nat Nanotechnol*. 2014; 9: 233-9.
41. Ku G, Zhou M, Song SL, Huang Q, Hazle J, Li C. Copper Sulfide Nanoparticles As a New Class of Photoacoustic Contrast Agent for Deep Tissue Imaging at 1064 nm. *ACS Nano*. 2012; 6: 7489-96.
42. Zhou Y, Wang DP, Zhang YM, Chitgupi U, Geng JM, Wang YH, et al. A Phosphorus Phthalocyanine Formulation with Intense Absorbance at 1000 nm for Deep Optical Imaging. *Theranostics*. 2016; 6: 688-97.
43. Jiang Y, Upputuri PK, Xie C, Lyu Y, Zhang L, Xiong Q, et al. Broadband Absorbing Semiconducting Polymer Nanoparticles for Photoacoustic Imaging in Second Near-Infrared Window. *Nano Lett*. 2017; DOI: 10.1021/acs.nanolett.7b02106.
44. Jiang TY, Sun WJ, Zhu QW, Burns NA, Khan SA, Mo R, et al. Furin-Mediated Sequential Delivery of Anticancer Cytokine and Small-Molecule Drug Shuttled by Graphene. *Adv Mater*. 2015; 27: 1021-8.
45. Min YZ, Li JM, Liu F, Yeow EKL, Xing BG. Near-Infrared Light-Mediated Photoactivation of a Platinum Antitumor Prodrug and Simultaneous Cellular Apoptosis Imaging by Upconversion-Luminescent Nanoparticles. *Angew Chem Int Ed*. 2014; 53: 1012-6.
46. Kairdolf BA, Smith AM, Stokes TH, Wang MD, Young AN, Nie SM. Semiconductor Quantum Dots for Bioimaging and Biodiagnostic Applications. *Annu Rev Anal Chem*. 2013; 6: 143-62.
47. Song XR, Wang XY, Yu SX, Cao JB, Li SH, Li J, et al. Co<sub>3</sub>Se<sub>8</sub> Nanoplates as a New Theranostic Platform for Photoacoustic/Magnetic Resonance Dual-Modal-Imaging-Guided Chemo-Photothermal Combination Therapy. *Adv Mater*. 2015; 27: 3285-91.
48. Yin WY, Yan L, Yu J, Tian G, Zhou LJ, Zheng XP, et al. High-Throughput Synthesis of Single-Layer MoS<sub>2</sub> Nanosheets as a Near-Infrared Photothermal-Triggered Drug Delivery for Effective Cancer Therapy. *ACS Nano*. 2014; 8: 6922-33.
49. Cheng L, Liu JJ, Gu X, Gong H, Shi XZ, Liu T, et al. PEGylated WS<sub>2</sub> Nanosheets as a Multifunctional Theranostic Agent for in vivo Dual-Modal CT/Photoacoustic Imaging Guided Photothermal Therapy. *Adv Mater*. 2014; 26: 1886-93.
50. Kong LD, Xing LX, Zhou BQ, Du LF, Shi XY. Dendrimer-Modified MoS<sub>2</sub> Nanoflakes as a Platform for Combinational Gene Silencing and Photothermal Therapy of Tumors. *ACS Appl Mater Inter*. 2017; 9: 15995-6005.
51. Wang SG, Li X, Chen Y, Cai XJ, Yao HL, Gao W, et al. A Facile One-Pot Synthesis of a Two-Dimensional MoS<sub>2</sub>/Bi<sub>2</sub>S<sub>3</sub> Composite Theranostic Nanosystem for Multi-Modality Tumor Imaging and Therapy. *Adv Mater*. 2015; 27: 2775-82.
52. Huang GM, Zhu XL, Li H, Wang LR, Chi XQ, Chen JH, et al. Facile Integration of Multiple Magnetite Nanoparticles for Theranostics Combining Efficient MRI and Thermal Therapy. *Nanoscale*. 2015; 7: 2667-75.
53. Du M, Li CP, Chen M, Ge ZW, Wang X, Wang L, et al. Divergent Kinetic and Thermodynamic Hydration of a Porous Cu(II) Coordination Polymer with Exclusive CO<sub>2</sub> Sorption Selectivity. *J Am Chem Soc*. 2014; 136: 10906-9.
54. Gyawali D, Zhou S, Tran RT, Zhang Y, Liu C, Bai X, et al. Fluorescence Imaging Enabled Biodegradable Photostable Polymeric Micelles. *Adv Healthcare Mater*. 2014; 3: 182-6.
55. Ho YJ, Chang YC, Yeh CK. Improving Nanoparticle Penetration in Tumors by Vascular Disruption with Acoustic Droplet Vaporization. *Theranostics*. 2016; 6: 392-403.
56. Habash RW, Bansal R, Krewski D, Alhafid HT. Thermal Therapy, Part 1: An Introduction to Thermal Therapy. *Crit Rev Biomed Eng*. 2006; 34: 459-89.
57. Roti JLR. Cellular Responses to Hyperthermia (40-46 °C): Cell Killing and Molecular Events. *Int J Hyperther*. 2008; 24: 3-15.
58. Kircher MF, de la Zerde A, Jokerst JV, Zavaleta CL, Kempen PJ, Mittra E, et al. A Brain Tumor Molecular Imaging Strategy Using a New Triple-Modality MRI-Photoacoustic-Raman Nanoparticle. *Nat Med*. 2012; 18: 829-34.
59. [Internet] Reference Ranges of Hematology Data of Healthy Male BALB/c Nude Mice were Obtained From Charles River Laboratories: [http://www.criver.com/files/pdfs/rms/balbc-nude/rm\\_rm\\_r\\_balb-c\\_nude\\_mouse\\_clinical\\_pathology\\_data.aspx](http://www.criver.com/files/pdfs/rms/balbc-nude/rm_rm_r_balb-c_nude_mouse_clinical_pathology_data.aspx)